


RESEARCH ARTICLE | APRIL 23 2024

The role of permeability in lid-driven cavity flow containing a cluster of hot solids

Yunxin Zhang (张鑫鑫); Chenggong Li (李承功); Mao Ye (叶茂) *Physics of Fluids* 36, 043328 (2024)<https://doi.org/10.1063/5.0200388>

Articles You May Be Interested In

Motion of a two-dimensional neutrally buoyant circular particle in two-sided lid-driven cavity flow with thermal convection

Physics of Fluids (December 2023)

Perspectives on local thermal non-equilibrium (LTNE) Darcy–Bénard convection: Variable permeability and viscosity effects

Physics of Fluids (October 2024)

Thermal enhancement of couple stress fluid flow through anisotropic porous media

Physics of Fluids (April 2024)

**Physics of Fluids**

Special Topics Open for Submissions

[Learn More](#)

The role of permeability in lid-driven cavity flow containing a cluster of hot solids

Cite as: Phys. Fluids **36**, 043328 (2024); doi: [10.1063/5.0200388](https://doi.org/10.1063/5.0200388)

Submitted: 26 January 2024 · Accepted: 6 April 2024 ·

Published Online: 23 April 2024



View Online



Export Citation



CrossMark

Yunxin Zhang (张望鑫),^{1,2} Chenggong Li (李承功),¹ and Mao Ye (叶茂)^{1,a)}

AFFILIATIONS

¹National Engineering Research Center of Lower-Carbon Catalysis Technology, Dalian Institute of Chemical Physics, Chinese Academy of Sciences, Dalian 116023, China

²University of Chinese Academy of Sciences, Beijing 100049, China

^{a)}Author to whom correspondence should be addressed: maoye@dicp.ac.cn

ABSTRACT

The flow behavior of particle clusters with thermal convection in confined fluid flow has garnered considerable attention. One of the remaining challenges is to understand the role of a porous structure of particle clusters in the confined thermal fluid flow. In present work, a numerical study based on a double distribution function lattice Boltzmann model has been conducted to unveil the two-sided lid-driven cavity flow containing a hot cluster formed by an array of center-placed solids. First, we investigated the heat transfer by varying the Richardson number (Ri , from 0.01 to 1.0) and the solid fraction of the cluster (ϕ , from 0.0143 to 0.6734) with fixed cavity Reynolds number ($Re = 1000$) and Prandtl number ($Pr = 0.7$). The increase in Ri would lead to the formation of non-centrosymmetric streamlines and isotherms and an increase in the total averaged Nusselt number \overline{Nu}_a , in which several vortex structures being identified at high Ri and ϕ . Then, we explored the influence of permeability, quantified by the Darcy number (Da), by changing the porous structure of cluster via rearranging the array of solids. It is found that a higher permeability could enhance heat transfer of particle cluster due to the increase in convection, but the smaller surface area of solid particles would limit heat transfer. A correlation of \overline{Nu}_a with respect to Ri and Da could be developed based on our two-dimensional simulation results, allowing the evaluation of involved interplay between the porous structure of particle cluster and thermal convection in confined flow via a simple yet effective way.

Published under an exclusive license by AIP Publishing. <https://doi.org/10.1063/5.0200388>

I. INTRODUCTION

The confined thermal particulate two-phase flow is of practical importance in many industrial processes, for example, pulverized coal combustion,¹ rotary kiln,² and mixing tank.³ As frequently observed, the particles, rather than behaving as individual solids, always form agglomerates or clusters in the confined two-phase devices due to the particle–fluid interactions, which significantly influence the momentum and heat transfer between particles and surrounding fluid flows.^{4–6} Understanding the thermal particulate two-phase flow in confined setup, therefore, demands fundamental yet insightful study.

In order to understand the mechanism underlying the heat transfer performance of the particle clusters, numerous studies have been conducted. The particle aggregations are usually treated as a single cluster of particles.^{7–11} In these cases, the characteristic parameters, for example, the porosity, Reynolds number, and Prandtl number, were typically analyzed to unveil the heat transfer performance of the clusters either qualitatively or quantitatively. For the particle-assembled porous clusters, the group of particles behaves similarly to a solid

particle for a high solid fraction (or low porosity), while each particle is similar to an isolated body for a low solid fraction.¹² Wang *et al.*¹³ studied the convection heat transfer of the cluster of particles in the circulating fluidized bed riser. They found that the increase in porosity of the cluster and Reynolds number could enhance the heat transfer coefficients, and the downward moving cluster shows higher heat transfer coefficients than the upward moving one. Wittig *et al.*¹⁴ investigated the heat transfer characteristics of the clusters constructed with several spherical or cubical particles, and their results showed that the shape of the particles has little relevance to the temperature distribution of the cluster. For high Re , the Nusselt number could be enhanced with the increase in porosity because of the dramatic increase in temperature and velocity gradients inside the cluster. They also developed the relationships between the Nusselt number and Re and porosity. It is worth noting that varying the temperature could induce the change in the properties of the fluid flow, which further affects the momentum and heat transfer between the particles and fluid flow.^{15,16} Tang *et al.*¹⁷ simulated the flow passing through the 10×10 array of cylinders at

$Re = 100$ with the effect of opposing buoyancy. The results showed that the averaged Nusselt number of the high solid fraction array is enhanced at first but then decreases with the increase in Richardson number Ri , as for the lower solid fraction, the averaged Nusselt number nearly linearly decreases with the increase in Ri . Fu *et al.*¹⁸ implemented a particle-resolved direct numerical simulation to study the heat convection of fluid flow with temperature-dependent properties. They examined the fluid flow pass through the clusters constructed by randomly distributed sub-particles and preliminarily modeled the sub-grid heat transfer corrections of the cluster with the influence of heterogeneity.

However, the aforementioned studies mostly focus on the heat transfer of particle clusters in fluid flow without considering confinement effects. In fact, it is a non-trivial task to account for the confinement effects encountered in practical two-phase flow setups due to the complex geometry and involved boundary conditions. The lid-driven cavity flow has long been considered as an ideal confined fluid flow model. This is because, despite the simple geometry, the lid-driven cavity flow exhibits numerous fluid flow phenomena only found in the confined flows.¹⁹ Therefore, heat transfer in cavity flow has received considerable attention so far. For example, Khanafer *et al.*²⁰ studied the mixed convection in a lid-driven cavity with two cylinders, and Gangawane *et al.*^{21,22} investigated the mixed convection in a lid-driven cavity with a triangular block. The results showed that the insertion of obstacles in the confined flow could significantly affect the fluid flow and heat transfer. Later on, the porosity of the obstacles in the cavity has been researched. As reported, Taghizadeh and Asaditaheri²³ investigated the heat transfer in an inclined lid-driven cavity with a circular porous cylinder using the volume-averaged theory. Kashyap and Dass²⁴ studied a two-sided lid-driven cavity with a porous blockage. Furthermore, the cavity flows with multi-bodies have been studied by some researchers. Merrikh and Lage²⁵ studied the natural convection in a cavity filled with several conducting rods and showed that the arrangement of the blocks dominant the flow patterns and affects the heat transfer across the cavity. Liu *et al.*²⁶ investigated the Rayleigh-Bénard convection in the cavity filled with solid obstacles and showed the non-monotonic variation of the Nusselt number with the decrease in porosity, due to the competition between flow coherence and porous structure resistance. It can be concluded that the porosity structure of the embodied obstacles would affect the fluid flow and heat transfer in the cavity. However, the role of the porous structure of particle clusters in fluid flow and heat transfer in lid-driven cavity flow is yet to be understood.

The purpose of the present work, therefore, is to conduct the fundamental research to understand the effects of permeability on the heat transfer and fluid flow around the particle cluster in the confined flow, and then build the mathematical model of heat transfer related to cluster in the particle-laden two-phase flows. For simplicity, we conducted the preliminary investigation of a cluster formed by an array of particles in different regular arrangements, which is located in the center of a two-dimensional two-sided lid-driven cavity with mixed convection. The two-dimensional study is conducted in the present work due to the high demand of computational sources of the three-dimensional simulations. As a preliminary work, the two-dimensional system, though simplified, could still reflect most of the physics encountered in the three-dimensional system.²⁷ Nevertheless, in the future the three-dimensional simulations will be conducted for a more detailed and quantitative analysis. A double distribution function lattice Boltzmann model is applied for the particle-resolved simulations. Essentially the influence of the

permeability of particle cluster on the patterns of fluid flow around and in the cluster as well as heat transfer are insightfully discussed.

II. PROBLEM FORMULATION

The setup of the system is depicted in Fig. 1. The two-dimensional two-sided lid-driven cavity, with the length and height of L , is filled with incompressible Newtonian fluid. The fluid is driven by the top and bottom walls with the speed of U in opposite directions. The fluid in the cavity is initially at a cold temperature $T_c = 0$, and the temperatures of the top and bottom walls keep at T_c while the left and right walls are adiabatic. The cluster assembled by an array of particles in a square arrangement is located in the center of the cavity, with a fixed size of $D = 0.4L$. The hot particles in the array maintains a high temperature of T_h on the surface. Hence, the fluid is heated by the cluster while cooled by the top and bottom walls, and the flow in the cavity is propelled by the driven walls and the thermal buoyant force. The cavity system is defined in a lattice unit in lattice Boltzmann method. The length x , the velocity u , and the temperature T are related to the physical units by $x = \frac{x_p L}{L}$, $u = \frac{u_p U}{U}$, and $T = \frac{T_p - T_{c,p}}{T_{h,p} - T_{c,p}}$, respectively, where the subscript p denotes the variables in the physical units and L and U are the reference length and reference velocity. Once the characteristic parameters are given, e.g., the cavity edge length and lid-driven velocity, the variables in the two units can be converted to each other. In addition, $T_h = 1$ and $T_c = 0$ are the reference high and low temperatures; thus, the temperature difference is $\Delta T = 1$. The heat transfer and fluid flow are quantified by the dimensionless numbers, namely, Reynolds number Re , Prandtl number Pr , and Richardson number Ri . They are written as

$$\begin{aligned} Re &= \frac{UL}{\nu}, \\ Pr &= \frac{\nu}{\alpha}, \\ Ri &= \frac{g\beta(T_h - T_c)L}{U^2}, \end{aligned} \quad (1)$$

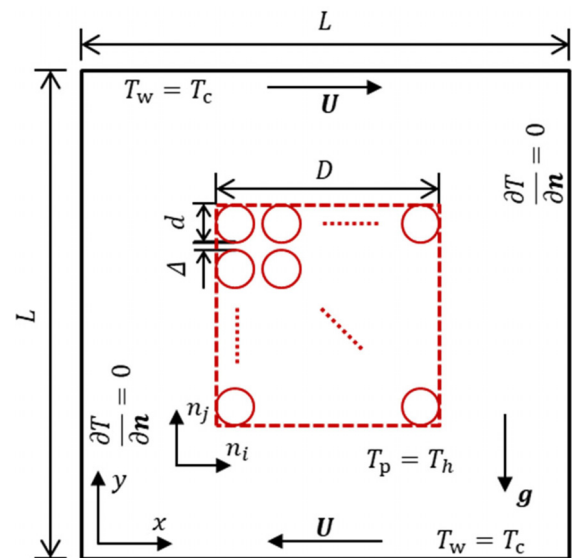


FIG. 1. Sketch of the two-dimensional two-sided lid-driven square cavity flow with a cluster formed by an array of center-placed solids.

TABLE I. The properties of the particle cluster.

Arrangement	NP	Δ/d	d/L	ϕ	ε	Da
Solid Rectangle	1×1	0.00	0.4000	1.0000	0.0000	0
Various particle sizes array (VSA)	5×5	0.10	0.0741	0.6734	0.3266	2.34×10^{-6}
	5×5	0.50	0.0571	0.4007	0.5993	2.43×10^{-5}
	5×5	1.00	0.0444	0.2424	0.7576	8.12×10^{-5}
	5×5	2.00	0.0308	0.1162	0.8838	2.69×10^{-4}
	5×5	5.00	0.0160	0.0314	0.9686	1.31×10^{-3}
	5×5	8.00	0.0108	0.0143	0.9857	3.02×10^{-3}
Various particle numbers array (VNA)	4×4	7.56	0.0150	0.0177	0.9823	3.79×10^{-3}
	5×5	5.42	0.0150	0.0276	0.9724	1.51×10^{-3}
	6×6	4.13	0.0150	0.0398	0.9602	7.00×10^{-4}
	8×8	2.67	0.0150	0.0707	0.9293	2.01×10^{-4}
	10×10	1.85	0.0150	0.1104	0.8896	7.21×10^{-5}
	15×15	0.83	0.0150	0.2485	0.7515	8.59×10^{-6}
	23×23	0.17	0.0150	0.5843	0.4157	2.63×10^{-7}

where ν and α are the kinematic viscosity and thermal diffusivity of fluid, respectively, β is the coefficient of thermal expansion, and g is the value of gravity acceleration. The dimensionless numbers reflect the characteristics of the fluid flow. The cavity Reynolds number Re is the ratio of the inertia to the viscosity of fluid flow. In the present work, it represents the magnitude of the force convection of the lid-driven cavity flow. The Prandtl number Pr is a dimensionless number describing the physical properties of the fluid flow, which is related to the heat convection. The Richardson number Ri reflects the relative strength of the natural convection induced by thermal buoyancy to the forced convection induced by cavity walls.

The porosity and permeability of the cluster, relating to the arrangements of primary solids and porous structures of the cluster, would also have significant effects on the fluid flow around and through the cluster. Various arrangements of the primary particles that assemble the clusters have been reported in previous works,^{13,14,18} e.g., the particles with a fixed size that arranged in concentric rings,¹² the particles with various sizes that arranged in a rectangular pattern.^{17,28,29} In the present work, the two kinds of particle arrangements are considered, namely, the various particle sizes array (VSA) and the various particle numbers array (VNA). In practical applications such as industrial catalytic processes, the catalyst particles are usually treated as spheres. Thus, the circular particles are selected as the primary solids to form the cluster. However, the clusters encountered in the industrial processes typically exhibit irregular shapes due to the complicated fluid-particle interactions. For simplicity, therefore, the rectangular cluster formed with circular primary solids, which has sharp corners and flat edges, leading to the rich phenomena of flow and heat transfer, is considered in this work. The particles are uniformly arranged as a center placed rectangular array, as shown in Fig. 1. In VSA, the primary particles (solid cylinders) are arranged as a 5×5 array with the varying diameter d . In VNA, the primary particles (solid cylinders) have a fixed size of $d = 0.015L$ and are placed as an $n_i \times n_j$ array, where $NP = n_i \times n_j$ denotes the number of primary particles. Thus, the gap between the adjacent particles Δ varies with the particle sizes and particle numbers for the VSA and the VNA, respectively.

The properties of the clusters are shown in Table I. The solid fraction is defined as the ratio of the total volume of the primary solids to the volume occupied by the rectangle cylinder with the edge length of D .²⁹ Thus, in the present work, the equation $\phi = NP \times \frac{1}{4}\pi d^2 / D^2$ is used to calculate the solid fraction, which stands for the proportion of the total area (or the total volume) of the primary particles $NP \times \frac{1}{4}\pi d^2$ in the area (or the volume) of the rectangular array enclosure (D^2). The porosity of the array enclosure is calculated by $\varepsilon = 1 - \phi$. Then the Darcy number of the cluster can be calculated by $Da = k/D^2 = d^2\varepsilon^3 / (180(1 - \varepsilon)^2 D^2)$, in which the permeability k represents the capability of the porous media to allow the fluid flow to pass through, while the Darcy number Da is the normalized permeability. The equation is known as the Carman-Kozeny equation,^{14,30} an empirical formula that correlates the permeability of the porous media to the solid fraction and specific surface, which is expected to be available in the two-dimensional configurations. Such an empirical equation is a prior value that depends on the porous media itself which is common in some research about particle-scale cluster^{14,31} as well as the numerical simulations in the REV scale.^{32,33} The solid fraction and permeability for either VNA or VSA can, thus, be obtained and are listed in Table I. Note the case of the single solid rectangle with the length of D is also simulated for comparison.

In addition, the heat transfer across the cavity flow is evaluated by the Nusselt number, which represents the dimensionless heat transfer rate, indicating the magnitude of convection heat transfer on the surface. First, the total (conduction and convection) heat flux (J)^{34–36} can be obtained as

$$J = \mathbf{u}(T - T_0) - \alpha \nabla T, \quad (2)$$

where \mathbf{u} is the local velocity, T is the local temperature of fluid flow, and T_0 denotes the reference temperature. Then, the local Nusselt number (Nu) along the cavity walls and particle surfaces can be calculated as

$$Nu = \frac{L}{\alpha(T - T_0)} J_n, \quad (3)$$

where J_n stands for the \mathbf{J} flux component on the normal direction n of the boundary. Then, the averaged Nusselt number (\overline{Nu}) on the boundary is defined by

$$\overline{Nu} = \frac{\int Nuds}{\int ds}, \quad (4)$$

where s denotes the surface of the boundary wall. To evaluate the heat transfer of the cluster quantitatively, the averaged Nusselt number $\overline{Nu}_{p,ij}$ based on each single particle is defined as

$$\overline{Nu}_{p,ij} = \frac{\int Nu_{p,ij} ds}{S_{ij}}, \quad (5)$$

where $Nu_{p,ij}$ is the local Nusselt number distribution of the individual particle in the array and the subscripts i and j indicate the number of row and column of the particles in the array as shown in Fig. 1. S_{ij} is the surface area of each particle. In addition, the heat transfer performance of the whole cluster is evaluated by the total averaged Nusselt number (\overline{Nu}_a) based on the surface of the array enclosure, which is calculated by

$$\overline{Nu}_a = \frac{1}{4D} \sum S_{ij} \overline{Nu}_{p,ij}, \quad (6)$$

where $4D$ is the surface area of the square array enclosure.

III. NUMERICAL METHOD

A. Thermal lattice Boltzmann equations

Here, the lattice Boltzmann model is adopted to investigate the mixed convection in the cavity flow due to its easy implementation, accuracy and natural parallelism.³⁷ Therefore, the single-relaxation-time double distribution function lattice Boltzmann equations based on the BGK approximation are implement to model the fluid flow and heat transfer in the cavity,³⁸ which is written as

$$f_i(\mathbf{r} + \mathbf{e}_i \delta_t, t + \delta_t) - f_i(\mathbf{r}, t) = -\frac{1}{\tau_f} [f_i(\mathbf{r}, t) - f_i^{eq}(\mathbf{r}, t)] + \delta_t F_i(\mathbf{r}, t), \quad (7)$$

$$g_i(\mathbf{r} + \mathbf{e}_i \delta_t, t + \delta_t) - g_i(\mathbf{r}, t) = -\frac{1}{\tau_g} [g_i(\mathbf{r}, t) - g_i^{eq}(\mathbf{r}, t)], \quad (8)$$

where $f_i(\mathbf{r}, t)$ and $g_i(\mathbf{r}, t)$ are the fluid particle distribution function and thermal energy distribution function at the position \mathbf{r} and time t , and τ_f and τ_g are the dimensionless relaxation time, respectively. F_i denotes the discrete body force term exerted on the fluid flow. The nine-velocities model (D2Q9) is implemented, and thus, the discrete velocities \mathbf{e}_i are

$$\mathbf{e}_i = \begin{cases} (0, 0) & i = 0, \\ c \left(\cos \left[(i-1) \frac{\pi}{2} \right], \sin \left[(i-1) \frac{\pi}{2} \right] \right) & i = 1-4, \\ \sqrt{2}c \left(\cos \left[(2i-1) \frac{\pi}{4} \right], \sin \left[(2i-1) \frac{\pi}{4} \right] \right) & i = 5-8, \end{cases} \quad (9)$$

where c is the lattice speed defined as the ratio of lattice length δ_x and time step δ_t , which is normally selected as $c = \delta_x / \delta_t = 1$.

Furthermore, $c_s = c/\sqrt{3}$ is the lattice sound speed. For the incompressible thermal fluid flow, the equilibrium distribution functions for f_i and g_i are adopted as follows:^{38,39}

$$f_i^{eq} = \omega_i \left[\rho + \rho_0 \left(3 \frac{\mathbf{e}_i \cdot \mathbf{u}}{c^2} + 4.5 \frac{(\mathbf{e}_i \cdot \mathbf{u})^2}{c^4} - 1.5 \frac{\mathbf{u}^2}{c^2} \right) \right], \quad (10)$$

$$g_i^{eq} = \begin{cases} \rho \omega_i E \left[-\frac{3\mathbf{u}^2}{2c^2} \right], & i = 0, \\ \rho \omega_i E \left[\frac{3}{2} + \frac{3\mathbf{e}_i \cdot \mathbf{u}}{2c^2} + \frac{9(\mathbf{e}_i \cdot \mathbf{u})^2}{2c^4} - \frac{3\mathbf{u}^2}{2c^2} \right], & i = 1-4, \\ \rho \omega_i E \left[3 + 6 \frac{\mathbf{e}_i \cdot \mathbf{u}}{c^2} + \frac{9(\mathbf{e}_i \cdot \mathbf{u})^2}{2c^4} - \frac{3\mathbf{u}^2}{2c^2} \right], & i = 5-8, \end{cases} \quad (11)$$

where the weight coefficients ω_i are written as $\omega_0 = 4/9$, $\omega_{1-4} = 1/9$, and $\omega_{5-8} = 1/36$. The mean density ρ_0 is set as 1. The macroscopic variables of fluid flow, i.e., velocity \mathbf{u} , density ρ and temperature T are defined as

$$\rho = \sum_{i=0}^8 f_i, \quad (12)$$

$$\rho_0 \mathbf{u} = \sum_{i=0}^8 \mathbf{e}_i f_i + \frac{\delta_t}{2} \mathbf{F}, \quad (13)$$

$$\rho RT = \sum_{i=0}^8 g_i, \quad (14)$$

where R is the gas constant which can be calculated by $c^2 = 3RT_0$ and $E = RT$, and T_0 is the mean temperature of fluid flow and is set as T_c . According to the discrete force scheme proposed by Guo *et al.*,⁴⁰ the macroscopic body force \mathbf{F} is implemented in Eq. (7) via

$$F_i(\mathbf{r}, t) = \left(1 - \frac{1}{2\tau_f} \right) \omega_i \left[3 \frac{\mathbf{e}_i \cdot \mathbf{u}}{c^2} + 9 \frac{(\mathbf{e}_i \cdot \mathbf{u})^2}{c^4} \right] \cdot \mathbf{F}. \quad (15)$$

In the present work, the body force \mathbf{F} is the thermal buoyant force which is modeled by the Boussinesq approximation

$$\mathbf{F}_B = -\rho_0 \mathbf{g} \beta (T - T_0), \quad (16)$$

where $T - T_0$ is the deviation of actual fluid temperature T from the reference temperature $T_0 = T_c$ and ρ_0 is the corresponding fluid density at T_0 .

The Chapman-Enskog expansion analysis bridges the lattice Boltzmann equations and macroscopic incompressible Navier-Stokes equations with the energy equation,^{38,39} then the relationship of the kinematic viscosity ν and relaxation time parameter τ_f , as well as the relationship of the thermal diffusivity α and relaxation time parameter and τ_g are given as

$$\nu = \frac{1}{6} (2\tau_f - 1), \quad (17)$$

$$\alpha = \frac{1}{3} (2\tau_g - 1). \quad (18)$$

B. Boundary treatment

The interactions of fluid flow and solids are implemented through the no-slip velocity boundary condition and constant temperature thermal boundary condition, namely, the Dirichlet boundary condition. For example, the treatment of the complex curve boundary

which does not conform to the Cartesian grid shape is shown in Fig. 2, the unknown distribution function $f_i(\mathbf{r}_f, t + \delta t)$ and $g_i(\mathbf{r}_f, t + \delta t)$ on the lattice node \mathbf{r}_f that linked by the wall node \mathbf{r}_w in the direction \mathbf{e}_i (i.e., $\mathbf{r}_f = \mathbf{r}_w + \mathbf{e}_i \delta t$) are to be determined to finish the streaming step. The curve boundary intersects with the link between \mathbf{r}_w and \mathbf{r}_f on boundary point \mathbf{r}_b , a parameter q is introduced to quantify the location of \mathbf{r}_b ,

$$q = \frac{|\mathbf{r}_f - \mathbf{r}_b|}{|\mathbf{r}_f - \mathbf{r}_w|}. \quad (19)$$

The non-equilibrium extrapolation method developed by Guo *et al.*⁴¹ is implemented. The fluid “fictitious” post collision density distribution function $f_i^+(\mathbf{r}_w, t)$ on \mathbf{r}_w can be calculated by decomposing the distribution function $f_i(\mathbf{r}_w, t)$ into its equilibrium and nonequilibrium parts

$$f_i^+(\mathbf{r}_w, t) = f_i^{\text{eq}}(\mathbf{r}_w, t) + \left(1 - \frac{1}{\tau_f}\right) f_i^{\text{neq}}(\mathbf{r}_w, t). \quad (20)$$

According to Eq. (10), the equilibrium part $f_i^{\text{eq}}(\mathbf{r}_w, t)$ is approximated by

$$f_i^{\text{eq}}(\mathbf{r}_w, t) = \omega_i \left[\bar{\rho}_w + \rho_0 \left(3 \frac{\mathbf{e}_i \cdot \bar{\mathbf{u}}_w}{c^2} + 4.5 \frac{(\mathbf{e}_i \cdot \bar{\mathbf{u}}_w)^2}{c^4} - 1.5 \frac{\bar{\mathbf{u}}_w^2}{c^2} \right) \right], \quad (21)$$

where the approximation density on \mathbf{r}_w is $\bar{\rho}_w = \rho(\mathbf{r}_f)$ and the approximation velocity can be determined by linear extrapolation

$$\bar{\mathbf{u}}_w = \begin{cases} \mathbf{u}_{w,1} & q \geq 0.75, \\ q\mathbf{u}_{w,1} + (1-q)\mathbf{u}_{w,2} & q < 0.75, \end{cases} \quad (22)$$

where $\mathbf{u}_{w,1}$ and $\mathbf{u}_{w,2}$ are two approximation velocities based on the extrapolation schemes depending on the velocity \mathbf{u}_f on the position \mathbf{r}_f and \mathbf{u}_{ff} on the position \mathbf{r}_{ff} as well as the boundary velocity \mathbf{u}_b on the boundary \mathbf{r}_b , i.e.,

$$\begin{cases} \mathbf{u}_{w,1} = \frac{\mathbf{u}_b + (q-1)\mathbf{u}_f}{q}, \\ \mathbf{u}_{w,2} = \frac{2\mathbf{u}_b + (q-1)\mathbf{u}_{\text{ff}}}{1+q}, \end{cases} \quad (23)$$

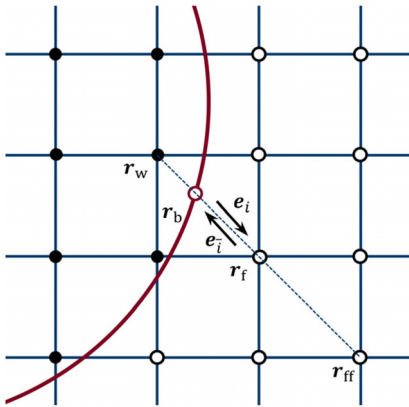


FIG. 2. Schematic of curve boundary treatment in the Cartesian grids.

In addition, the nonequilibrium part $f_i^{\text{neq}}(\mathbf{r}_w, t)$ is obtained by extrapolation

$$f_i^{\text{neq}}(\mathbf{r}_w, t) = \begin{cases} f_i^{\text{neq}}(\mathbf{r}_f, t) & q \geq 0.75, \\ qf_i^{\text{neq}}(\mathbf{r}_f, t) + (1-q)f_i^{\text{neq}}(\mathbf{r}_{\text{ff}}, t) & q < 0.75. \end{cases} \quad (24)$$

For the fixed wall, the wall and fluid nodes are invariable, and the boundary velocity $\mathbf{u}_b = 0$.

For the temperature field, the similar boundary condition treatment based on non-equilibrium extrapolation method⁴² is written as

$$g_i^+(\mathbf{r}_w, t) = g_i^{\text{eq}}(\mathbf{r}_w, t) + \left(1 - \frac{1}{\tau_g}\right) g_i^{\text{neq}}(\mathbf{r}_w, t), \quad (25)$$

where the equilibrium part $g_i^{\text{eq}}(\mathbf{r}_w, t)$ is determined according to Eq. (11), the approximation of density $\bar{\rho}_w$ and velocity $\bar{\mathbf{u}}_w$ are obtained previously, and the approximation of temperature is obtained by

$$\bar{T}_w = \begin{cases} T_{w,1} & q \geq 0.75, \\ qT_{w,1} + (1-q)T_{w,2} & q < 0.75, \end{cases} \quad (26)$$

$$\begin{cases} T_{w,1} = (T_b + (q-1)T_f)/q, \\ T_{w,2} = \frac{2T_b + (q-1)T_{\text{ff}}}{1+q}, \end{cases} \quad (27)$$

note $\rho\varepsilon = \rho RT$. The temperature of boundary T_b is a given constant for the Dirichlet boundary condition. In addition, the nonequilibrium part $g_i^{\text{neq}}(\mathbf{r}_w, t)$ is obtained by

$$g_i^{\text{neq}}(\mathbf{r}_w, t) = \begin{cases} g_i^{\text{neq}}(\mathbf{r}_f, t) & q \geq 0.75, \\ qg_i^{\text{neq}}(\mathbf{r}_f, t) + (1-q)g_i^{\text{neq}}(\mathbf{r}_{\text{ff}}, t) & q < 0.75. \end{cases} \quad (28)$$

Moreover, the non-equilibrium extrapolation method is also implemented for the boundary condition on cavity wall.^{43,44} Note the Neumann thermal boundary condition is implemented for the adiabatic side walls, and the wall temperature is predetermined by second-order discretization⁴²

$$T_w = \frac{1}{3} \left(4T_f - T_{\text{ff}} - 2 \left(\frac{\partial T}{\partial n} \right)_i |\mathbf{e}_i| \delta t \right), \quad (29)$$

where n denotes the normal direction of the boundary wall and $\frac{\partial T}{\partial n}$ equals to zero for the adiabatic wall.

IV. VALIDATION

A. Model validation

In order to validate the accuracy of the numerical method, the natural convection in a square cavity that contains an isothermally heated cylinder is simulated. The cylinder of diameter $D = 0.4L$ is located at the position of $(0.5L, 0.6L)$, where $L = 500$ is the cavity length. The velocity of fluid flow satisfies the non-slip boundary condition on the cavity walls and cylinder surface. In addition, the side walls of the cavity are kept at temperature $T_c = 0$, and the top and bottom walls are adiabatic. The surface temperature of cylinder maintains $T_h = 1$, which heats the surrounding fluid and propels the natural convection. The dimensionless parameters, i.e., the Rayleigh number and Prandtl number, are set as $Ra = g\beta(T_h - T_c)L^3/\nu\alpha = 10^6$ and $Pr = 10$, according to the various previous works.^{45,46}

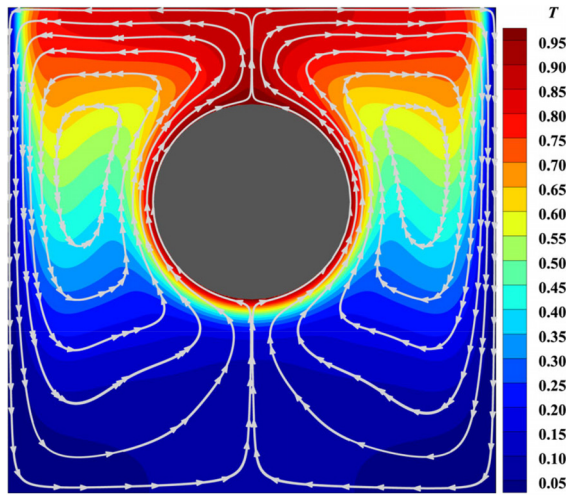


FIG. 3. The streamlines and isotherms at steady state of the natural convection in the square cavity with the hot cylinder.

As shown in Fig. 3, the streamlines and isotherms at steady state present axisymmetric distributions due to the axisymmetric setup. The propelled fluid flow forms two vortices at the left and right side of the cylinder owing to the buoyancy effect, while the high-temperature area is over the cylinder and the low-temperature area is below the cylinder. The results show good agreement with Refs. 45 and 46. Moreover, the local Nusselt numbers along the sidewall (Nu_w) and half cylinder circumference (Nu_θ) are calculated according to Eq. (3) as shown in Fig. 4. The high values of Nu_w and Nu_θ on the top of the sidewall and bottom of the cylinder surface also indicate the high temperature gradients, which is consistent with the isotherms in Fig. 3. The quantitative consistency validates the accuracy of the numerical method.

B. Grid independence

To validate the grid independence of the numerical model, the mixed convection in the cavity containing the cluster is investigated by various grid sizes. The cluster of VSA with $D = 0.4L$ and $\phi = 0.2424$

TABLE II. Comparisons of the averaged Nusselt numbers of the particles for different grid size cases.

Geometry	Grid size	Ri	\overline{Nu}_p
VSA $\phi = 0.2424$	500 × 500	0.00	2.253
	750 × 750	0.00	2.267
	1000 × 1000	0.00	2.278
	1250 × 1250	0.00	2.286
	500 × 500	1.00	7.491
VNA $\phi = 0.5843$	750 × 750	1.00	7.572
	1000 × 1000	1.00	7.617
	1250 × 1250	1.00	7.645
	500 × 500	0.00	0.307
	750 × 750	0.00	0.315
	1000 × 1000	0.00	0.320
	1250 × 1250	0.00	0.322
	500 × 500	1.00	0.647
	750 × 750	1.00	0.665
	1000 × 1000	1.00	0.674
	1250 × 1250	1.00	0.678

and the cluster of VNA with $D = 0.4L$ and $\phi = 0.5843$ are considered, with the cavity length being divided into 500, 750, 1000, and 1250 grids. The typical dimensionless numbers of the cavity fluid flow are $Re = 1000$, $Pr = 0.7$, and $Ri = 0$ or 1. Table II shows the computational results of various mesh grids. The averaged Nusselt numbers on the particle surface \overline{Nu}_p are calculated, which shows the consistency across different grid sizes, and indicates the reliability of the simulation. The relative deviation of the averaged Nusselt number is less than 0.4% for the VSA and less than 0.7% for the VNA when $L = 1000$, compared to the situations with smaller grid size. In addition, the velocity profile along the vertical centerline of the cavity flow containing VNA with $\phi = 0.5843$ and $Ri = 0.01$ is obtained (see Fig. 5). It shows that the results of $L = 1000$ is consistent with the results with finer mesh grid. Hence, $L = 1000$ is chosen to save the computing time and assure the accuracy and efficiency of the simulations. Such

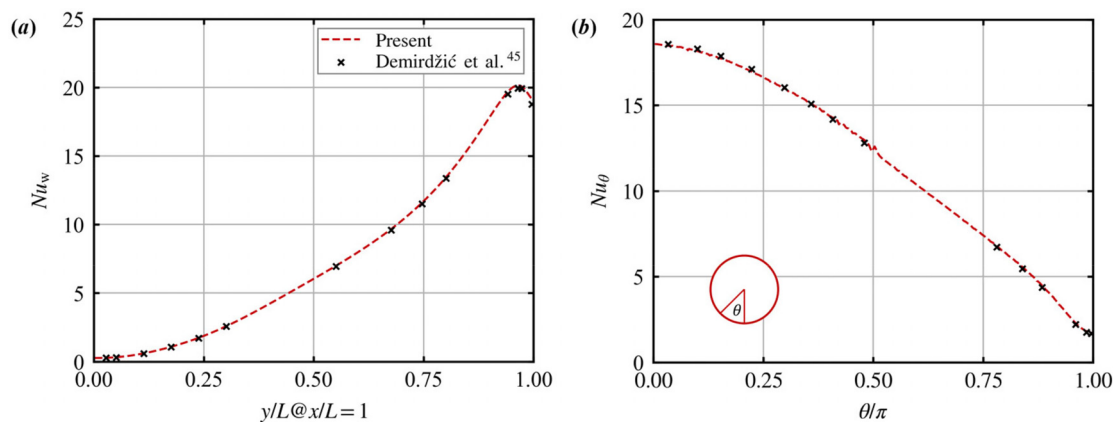


FIG. 4. The local Nusselt numbers variation along: (a) the sidewall and (b) the cylinder surface, compared to the results of Demirdžić et al.⁴⁵

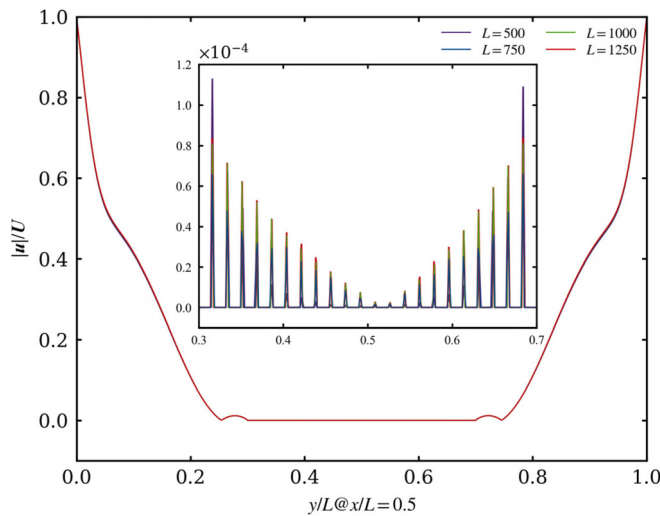


FIG. 5. The normalized velocity distribution along $x/L = 0.5$ of the cavity flow containing VNA with $\phi = 0.5843$ and $Ri = 0.01$. The positions within the cluster correspond to $y/L = 0.3$ – 0.7 .

mesh grid also ensures the fully-resolved simulations in which the particles are resolved by at least 15 grids.

V. RESULTS AND DISCUSSION

In this section, the simulations are conducted focusing on the fluid flow and heat transfer in the two-sided lid-driven cavity containing a cluster of particle array with various arrangements and solid fractions. The Richardson number of the cavity flow is set as $Ri = 0.01$ – 1.00 . Since the different arrangements of VSA and VNA are adopted, the corresponding solid fraction of cluster is $\phi = 0.0143$ – 0.6734 , note $\phi = 1$ represents the case of single solid rectangle. The Reynolds number and the Prandtl number of the cavity flow are fixed at $Re = 1000$ and $Pr = 0.7$, respectively. The speed of driven wall is selected as $U = 0.05$, and the viscosity and thermal diffusion coefficient are $\nu = 0.05$ and $\alpha = 0.0714$, respectively.

The convergence criteria are essentially applied to evaluate whether the deviations of the velocity and temperature of fluid flow at the consequent time steps are lower than a pre-defined threshold for terminating the simulation. Note that the velocity field is vector field, a normalized L2-norm form as shown in Eq. (30) is usually implemented as the convergence criteria according to Guo *et al.*⁴⁰

$$Err_u = \frac{\sqrt{\sum_r (\mathbf{u}(\mathbf{r}, t) - \mathbf{u}(\mathbf{r}, t - \delta t))^2}}{\sqrt{\sum_r \mathbf{u}(\mathbf{r}, t)^2}} < \epsilon_u. \quad (30)$$

As the temperature field is a scalar field, a normalized L1-norm is adopted following Ref. 47

$$Err_T = \frac{\sum_r |T(\mathbf{r}, t) - T(\mathbf{r}, t - \delta t)|}{\sum_r |T(\mathbf{r}, t)|} < \epsilon_T, \quad (31)$$

which could accelerate the convergence. In this work, the convergence criteria Eqs. (30) and (31) are, respectively, used for velocity and

temperature field simulation with $\epsilon_u = \epsilon_T = 10^{-8}$. The evolutions of Err_u and Err_T with time indicate the simulations are converged, and the fluid flow and temperature fields could reach the steady state.

A. Flow patterns and temperature fields

The fluid flow and temperature fields in the cavity are discussed in this section. Figure 6 shows the streamlines and isotherms of the cavity flow with the cluster at high ϕ . For example, the results of the VSA with $\phi = 0.6734$ are depicted in Figs. 6(a)–6(c). For $Ri = 0.01$ as shown in Fig. 6(a), the isotherms and streamlines exhibit annular distributions around the cluster, with two corner eddies observed in the top-left and bottom-right corners of the cavity can be observed. The centrosymmetry of the flow patterns indicates that the lid-driven forced convection is dominant, while the buoyancy effect is low due to the small Ri . In addition, the internal fluid flow within the cluster is too weak to be observed, which could be ascribed to the low porosity of the cluster. The separations of the fluid flow can be observed near the corner particles. This can be ascribed to the rectangular arrangement of the particles, which creates the sharp corner of the cluster.^{48,49} Moreover, a pair of vortex structures with similar shapes located over or below the cluster are formed, which indicates the dominant effect of centrosymmetric forced convection. As the increase in Ri up to 0.25 according to Fig. 6(b), the flow field in the cavity becomes asymmetric by the increase in buoyancy effect. The top-left corner eddy expands while the bottom-left one shrinks. An extra vortex structure appears at the right side of the array, this could be ascribed to the competition of the rising flow due to the buoyancy effect near the cluster and the downward flow near the cavity wall. Meanwhile, the streamlines at the left side of the cluster attach to the body, which is induced by the upward buoyancy and fluid flow. Such flow patterns indicate that the aiding buoyancy delays the flow separation while the opposing buoyancy results in a wider wake for the flow passing the heated particles, which is qualitatively coincident with that of flow around a single circular or rectangular cylinder.^{50,51} In addition, the vortex structure above the cluster shrinks while the one below expands. This indicates that the convection effect near the bottom wall is higher compared with that near the top wall, which enhances the separation of the flow. For $Ri = 1$ as shown in Fig. 6(c), the fluid flow is hard to pass through the cluster and forms several small vortex structures around the cluster. This could attribute to the mixed convection in the cavity flow, which consists of the buoyant effect induced natural convection and the lid-driven induced forced convection. With the increase in Ri , the upward flows are enhanced by the thermal buoyancy. Then, the fluid flows are confined and propelled by the cavity walls, leading to the formation of the complex vortex structures. Furthermore, for the same Ri , according to each column in Fig. 6, the streamlines and isotherms of the VSA ($\phi = 0.6734$), the VNA ($\phi = 0.5843$) and the solid rectangle ($\phi = 1$) are similar with each other. Hence, the solid fractions with the high values have little effects on the fluid flow and heat transfer, indicating that the cluster behaves similarly to a single solid particle.

On the other hand, the lower solid fraction could lead to different heat and fluid flows in cavity depending on various Ri . The results of the VSA with $\phi = 0.1162$ and the VNA with $\phi = 0.1104$ are shown in Fig. 7. For $Ri = 0.01$ according to Figs. 7(a) and 7(d), the annular distribution of the streamlines and isotherms of the bulk of the cavity

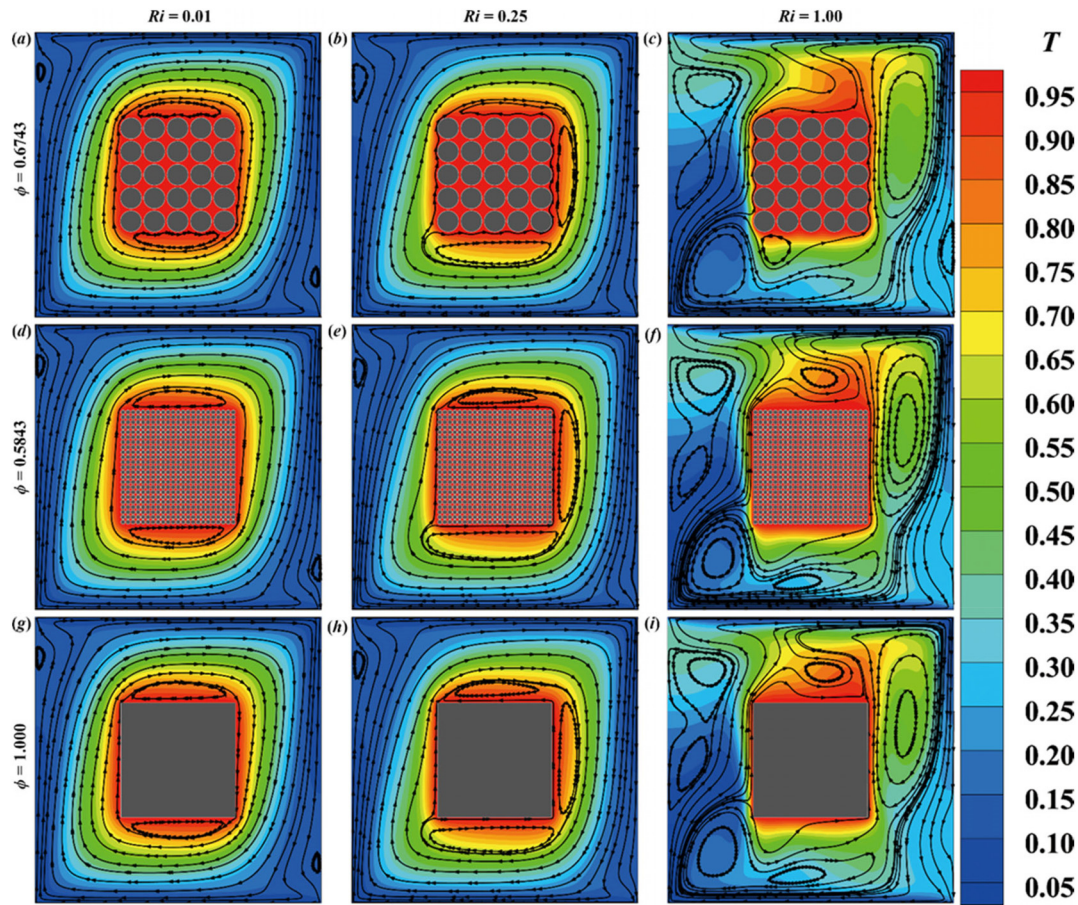


FIG. 6. The streamlines and isotherms in the two-sided lid-driven cavity flow containing a cluster with various arrangements: [(a)–(c)] VSA ($\phi = 0.6734$) at $Ri = 0.01, 0.25$, and 1.0 ; [(d)–(f)], VNA ($\phi = 0.5843$) at $Ri = 0.01, 0.25$ and 1.0 ; and [(g) and (h)] the solid rectangle ($\phi = 1$) at $Ri = 0.01, 0.25$, and 1.0 .

flow are similar to those of the higher ϕ cases. Nevertheless, the low ϕ , namely, the high porosity could induce the fluid to penetrate through the cluster, enhancing the permeability. The internal fluid swirls in the array enclosure, and isolates with the external streamlines. This indicates the domination of centrosymmetric lid-driven forced convection effect with negligible buoyancy. As the Ri increases up to 0.25 , as shown in Figs. 7(b) and 7(e), the thermal buoyancy is enhanced, resulting in the streamlines crossing the array enclosure and the breaking of the symmetry of the fluid flow. Hence the heat convection in the cluster is improved and the heat is taken out of the array enclosure, causing the further heated of fluid flows surrounding the cluster. Then, when $Ri = 1.0$ as shown in Figs. 7(c) and 7(f), the upward convection is dominant in the cavity flow, and the development of thermal plume over the cluster can be observed. This can be attributed to the permeability of the cluster further enhanced the upward convection in the array, which is also supported by Kashyap and Dass.²⁴

B. Heat transfer characteristics

The evolution of flow and temperature fields with various Ri and ϕ suggests the differences in the heat transfer characteristics of the

cavity flow. To quantitatively evaluate the heat transfer performance of the particle cluster, the averaged Nusselt numbers are calculated for the clusters with different ϕ at various Ri .

1. The effects of the Richardson number

Figure 8 shows the total averaged Nusselt numbers of the cluster as a function of Ri at various ϕ . The \overline{Nu}_a increases with the rise in Ri , exhibiting a particularly sharp increase when Ri is around 0.4 . This indicates that, as Ri increases from 0.01 , the buoyant effect gradually becomes dominant in the cavity flow compared to the lid-driven forced convection, promoting the convection within the cluster. However, after Ri is around 0.8 , the \overline{Nu}_a grows slowly. It is widely reported that the averaged Nusselt number of the particle could be improved with the increase in Ri for the uniform flow passing through the fixed particle.^{52,53} The reason is that the buoyancy effect, which is enhanced with Ri , accelerates the fluid flow that passes by the particle. Hence, the heat convection on the surface of the particle is enhanced, leading to the increase in the particle Nusselt number. In the present work, however, the mixed convection occurs in the confined flow, in which the balance of heat transfer between the particles cluster and

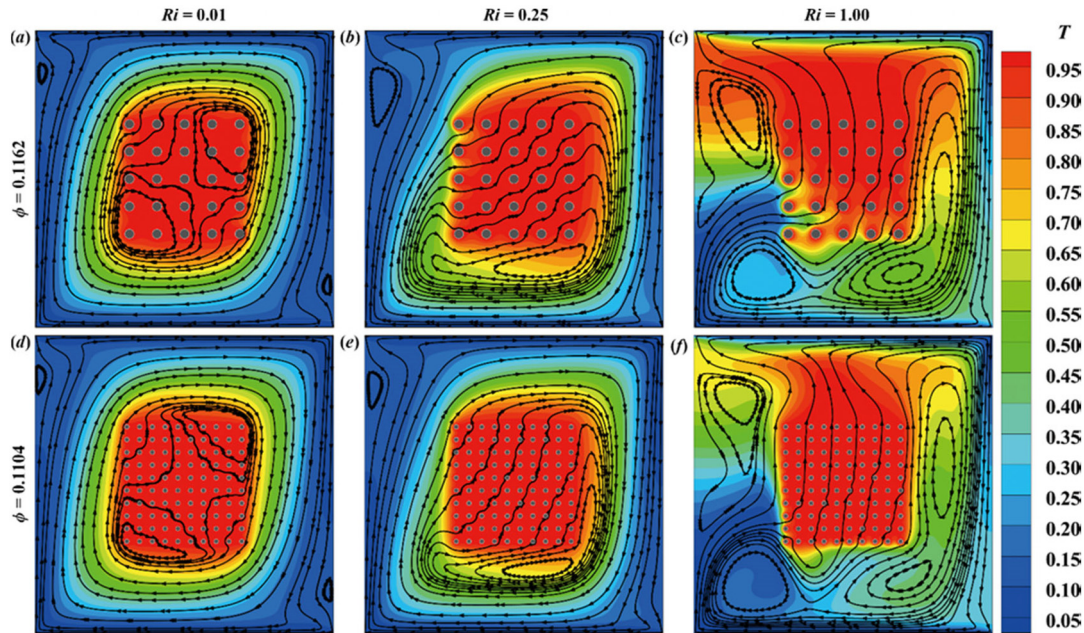


FIG. 7. The streamlines and isotherms in the two-sided lid-driven cavity flow with various arrangement: [(a)–(c)] VSA ($\phi = 0.1162$) at $Ri = 0.01, 0.25$, and 1.0 ; and [(d)–(f)] VNA ($\phi = 0.1104$) at $Ri = 0.01, 0.25$, and 1.0 .

cavity walls is eventually achieved. Although the heat convection is enhanced with the increase in Ri , it could be limited due to the constraint of the cavity walls. Then, the heat around the particle cluster cannot be efficiently transported out of the cavity, causing a higher temperature of the fluid flow around the particles to the cluster. Hence the temperature gradient around the particle cluster decreases, limiting the increase in \overline{Nu}_a .

2. The effects of the solid fraction and arrangements of the cluster

In order to further understand the effects of ϕ on the heat transfer of the cluster, the distribution of averaged Nusselt numbers $\overline{Nu}_{p,ij}$

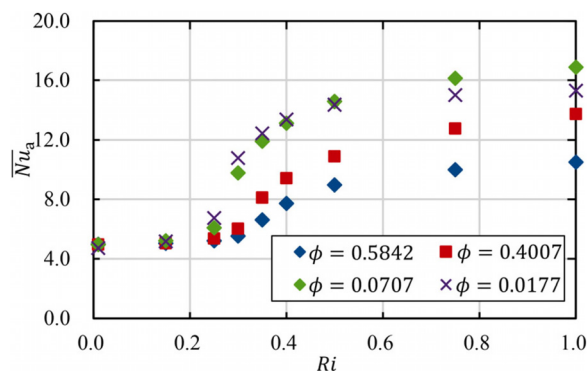


FIG. 8. The evolution of total averaged Nusselt number \overline{Nu}_a with Ri for the cluster with various ϕ .

of individual particles at various Ri is shown in Fig. 9. For the VNA with $\phi = 0.2485$ according to Figs. 9(a)–9(c), the averaged Nusselt numbers of the internal particles exhibit the near-zero values, while the higher averaged Nusselt numbers are observed for the particles at the periphery of the array, especially for the corner ones. This demonstrates the minimal contribution of the interior particles to the heat transfer of the cluster. The rectangular arrangement of array causes the high velocity and temperature gradients around the corner particles. Then the heat transfer is sharply enhanced, which is similar to the solid blockage reported by Islam *et al.*⁵⁴ As the increase in Ri from 0.01 to 1, the averaged Nusselt numbers for exterior particles increase significantly, but the interior ones still remain negligible. The low porosity limits the permeability of the cluster and suppresses the heat transfer of the interior particles, although the increased buoyancy enhances the convection and improves the heat transfer around the cluster. On the other hand, the results of the VSA with $\phi = 0.0143$ show differences according to Figs. 9(d)–9(f). Despite the low averaged Nusselt numbers of the interior particles for $Ri = 0.01$, they are of considerable values when the $Ri \geq 0.25$. It clearly demonstrates that the high porosity of the cluster enhances the heat transfer at high Ri . Due to the buoyancy induced natural convection at high Ri , the fluid flow passing through the array enclosure improves the heat transfer of the interior particles. Nevertheless, when the forced convection dominates in the cavity at $Ri = 0.01$, the swirling fluid flow within the cluster contributes slightly to the heat transfer of the internal particles, despite the high permeability of cluster.

Furthermore, the arrangements of the primary particles could also affect the heat transfer of the cluster. For example, the \overline{Nu}_a of the VSA and the VNA with various ϕ at $Ri = 0.25$ and $Ri = 0.5$ are shown in Fig. 10. For each arrangement, the \overline{Nu}_a is first enhanced but

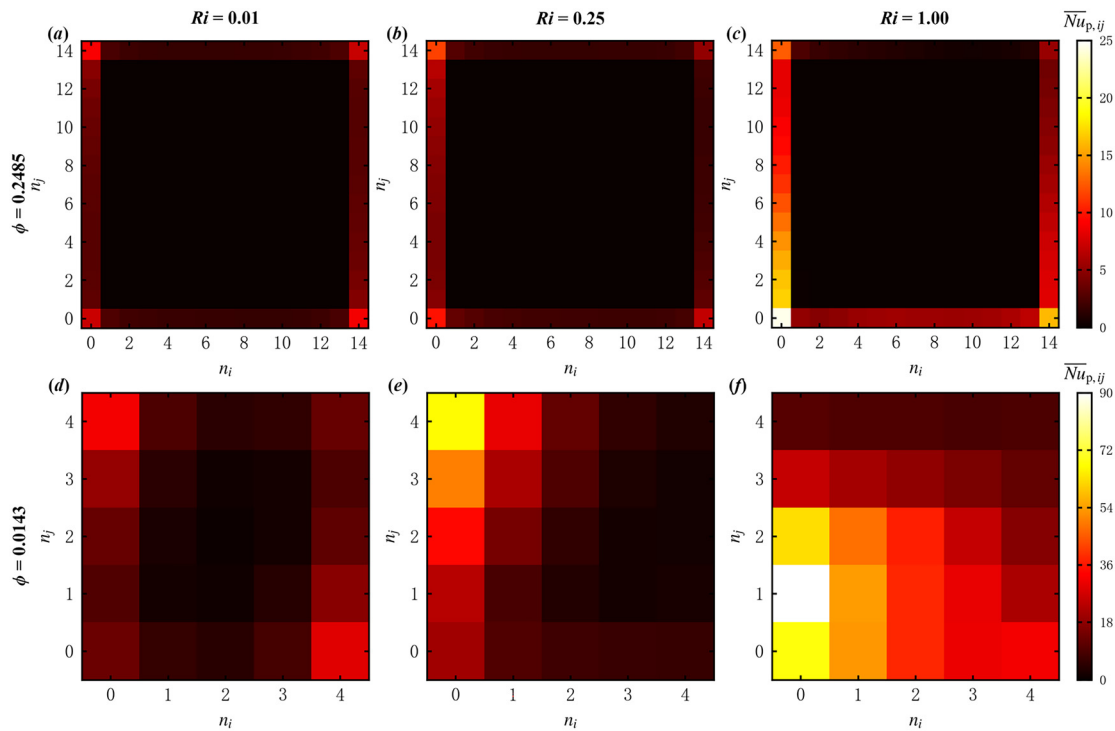


FIG. 9. The distribution of averaged Nusselt number $\overline{Nu}_{p,ij}$ of individual particles at various Ri for (a)–(c) the VNA with $\phi = 0.2485$; and (d)–(f) the VSA with $\phi = 0.0143$.

then decreased with the decrease in ϕ . However, the inconsistent trends of heat transfer performance of the cluster are observed for the VSA and VNA. According to the two cases marked ‘A’ in Fig. 10, the clusters of two arrangements with the similar solid fraction ($\phi = 0.1104$ for the VNA and $\phi = 0.1162$ for the VSA) yield two \overline{Nu}_a values that are significantly different. In contrast, for the two cases marked “B” in Fig. 10, the two clusters with different solid fractions ($\phi = 0.2485$ for the VNA and $\phi = 0.6734$ for the VSA) result in the similar values of \overline{Nu}_a . The results indicate that the solid fraction of the cluster is not the only parameter that determines the heat transfer of

the cluster, the arrangement of the array could also affect the pore-scale structure of the cluster, which influences the heat transfer.

In order to valid the effects of porous structure on the heat and fluid flow, simulations are implemented at the REV scale of a lid-driven cavity flow containing a square porous hot blockage. The numerical method is shown in the Appendix, and the code is validated in the previous work of the authors in the isothermal cases.^{55,56} The setup of the simulations can be referred in Fig. 1, note the particle cluster is replaced by a centerly placed square porous block with a length of D and a temperature of T_h . Some parameters of the simulations are listed: $Re = 1000$, $Pr = 0.7$, and $Ri = 0.5$. For simplicity, the ratio of the viscosities, thermal conductivities and thermal capabilities for the fluid flow and porous media as set as 1. The mesh grid is set as $L = 400$ for the efficiency of the simulations. Corresponding to the marked “A” and “B” cases in Fig. 10, four porous blockages with different solid fractions and permeabilities are considered, namely, A1): $\phi = 0.1104$, $Da = 7.21 \times 10^{-5}$; B1): $\phi = 0.1162$, $Da = 2.69 \times 10^{-4}$; A2): $\phi = 0.2485$, $Da = 8.59 \times 10^{-6}$; and B2): $\phi = 0.6732$, $Da = 2.34 \times 10^{-6}$.

The results of streamlines and isotherms are shown in Fig. 11, which depict similar flow patterns and temperature fields compared to the particle-resolved simulations. The fluid flow penetrates through or passes by the porous blockage, enhancing the heat convection in the cavity. In specific, the fluid flow enters the porous blockage from the left and bottom edges, and leaves from the top edge after being heated by the solid. Hence the plume can be observed over the blockage. Several vortex structures are formed around the porous blockage, which indicates the combination effect of the forced convection induced by the cavity walls and the natural convection induced by

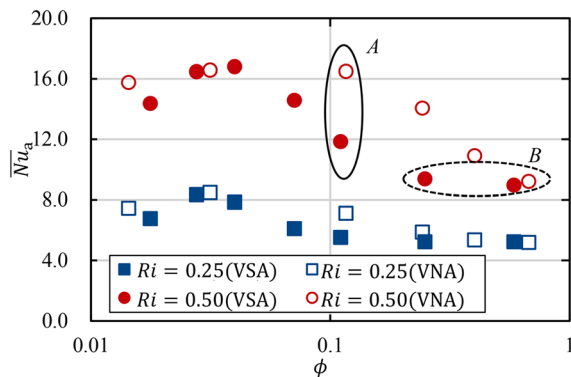


FIG. 10. The total averaged Nusselt number \overline{Nu}_a of the VSA and VNA with various ϕ at $Ri = 0.25$ and 0.5 .

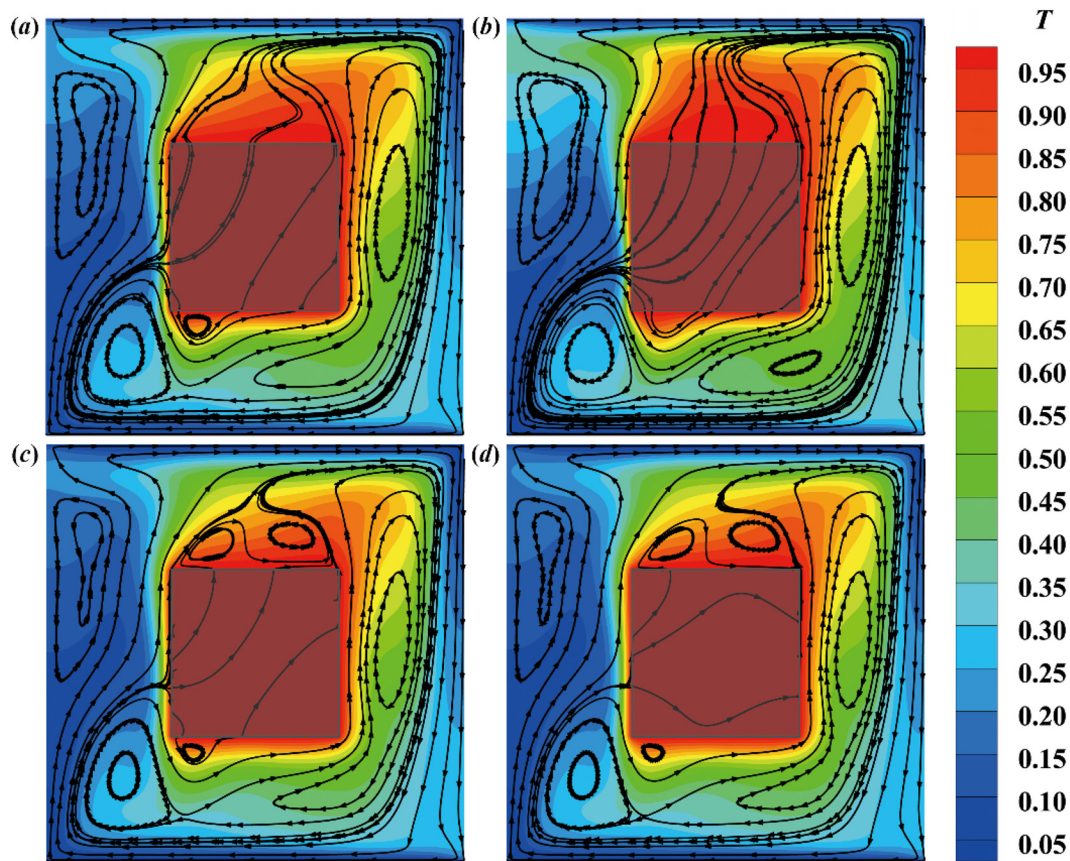


FIG. 11. The streamlines and isotherms in the two-sided lid-driven cavity flow with various solid fractions and permeabilities of the porous blockage: (a) $\phi = 0.1104$, $Da = 7.21 \times 10^{-5}$; (b) $\phi = 0.1162$, $Da = 2.69 \times 10^{-4}$; (c) $\phi = 0.2485$, $Da = 8.59 \times 10^{-6}$; and (d) $\phi = 0.6732$, $Da = 2.34 \times 10^{-6}$.

thermal buoyancy. According to Fig. 11, the streamlines and isotherms exhibit the dependencies on the Da of the porous blockage. For the low Da , the small vortex structures can be observed on the top edge of the porous blockage, as shown in Figs. 11(c) and 11(d). However, for the higher Da , for example, Fig. 11(b), the vortex structures cannot be formed. This indicates that the fluid flow penetrates the porous blockage more easily, which improves the heat convection in the porous blockage. Thus, the temperature of the fluid flow over the porous blockage is enhanced.

In order to analyze the effects of the porosity and permeability of the porous blockage on the heat transfer performance, the total averaged Nusselt number \overline{Nu}_a of the porous blockage is calculated, as shown in Fig. 12. Comparing the \overline{Nu}_a in group “A” and “B,” the heat transfer performance of the porous blockage can be significantly increased with the increase in Da . This can be attributed to the fluid flow penetrating the porous blockage which results in the stronger heat convection. However, the relationship between the \overline{Nu}_a and the solid fraction is not so significant. For the group “A,” the similar solid fractions of the two cases yield two significantly different \overline{Nu}_a values. In contrast, for the group “B,” the different solid fractions of the porous blockage result in the similar \overline{Nu}_a . This is consistent with the results in particle-resolved simulations as shown in Fig. 10, although the \overline{Nu}_a does not exhibit the quantitative consistency due to the different

setting of the simulations. Therefore, the solid fraction ϕ does not correlate well with the evolution of \overline{Nu}_a , while the Darcy number Da is expected to explain the variation of the \overline{Nu}_a .

Figure 13 shows the function of \overline{Nu}_a with respect to the Da at various Ri . For the lower Da , the increased permeability of the cluster could enhance the heat convection in the cluster which increases the

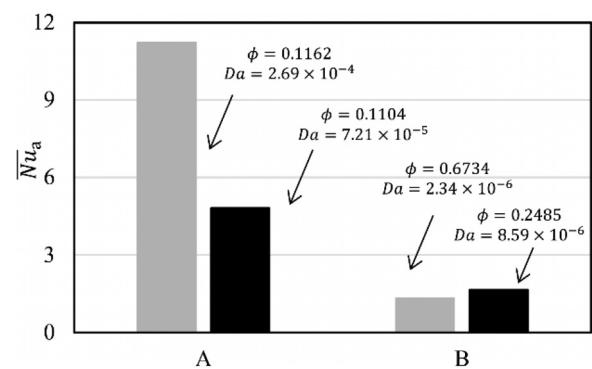


FIG. 12. The total averaged Nusselt number of the porous blockage with various solid fractions and permeabilities.

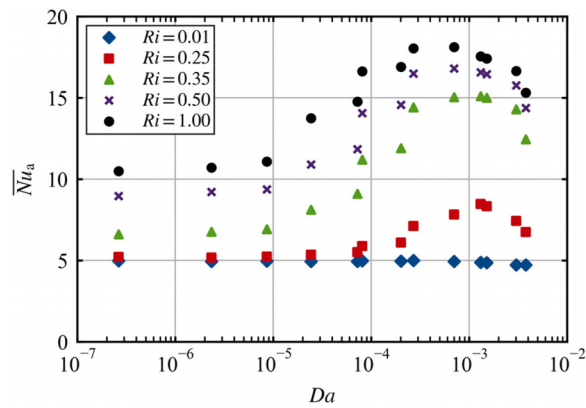


FIG. 13. The total averaged Nusselt number \overline{Nu}_a of the cluster with the variation of Da and Ri .

\overline{Nu}_a . However, the further increase in permeability at higher Da causes a decline of \overline{Nu}_a , indicating an optimal condition of permeability of the particle cluster which results in the highest heat transfer performance. In addition, the optimal Da decreases with the increase in Ri according to Fig. 13. This aspect will be further discussed later. In addition, for $Ri = 0.01$, the Da has little effects on the \overline{Nu}_a . This can be ascribed to the domination of the centrosymmetric forced convection within the cluster at the low Ri , which limits the heat transfer of interior particles. Furthermore, it is found that the Darcy number Da

correlates better with the variation of the total averaged Nusselt number of clusters compared to the solid fraction ϕ , according to Figs. 10 and 13. This indicates that the Da estimated by the Carman-Kozeny equation could reflect the geometry features of cluster, which significantly influence the heat and fluid flow.

To further understand the underlying mechanism of the variation in \overline{Nu}_a with Da , the heat and fluid flow around the cluster with different arrangements at $Ri = 0.5$ are illustrated in Figs. 14(a)–14(c). The orientations and lengths of the arrows represent the directions and magnitudes of the total heat flux \mathbf{J} that calculated by Eq. (2), providing a visualization of the heat convection.^{34,35} In addition, Fig. 14(d) shows the local Nusselt numbers Nu_a along the surface of the array enclosure, which present the heat transfer rate in the normal direction of the surface. A positive value of the local Nusselt number represents the output of heat from the cluster toward the surrounding fluid flow, while a negative value indicates the input of heat to the cluster. According to Fig. 14, the variation of the isotherms and \mathbf{J} fluxes demonstrate different heat transfer processes. For the VNA with $\phi = 0.1104$ ($Da = 7.21 \times 10^{-5}$), the magnitudes of the \mathbf{J} fluxes within the cluster are significantly weaker, indicating that the heat transfer process mainly occurs in the surrounding fluid flow of the cluster. The negligible heat transferred out of the cluster causes the lower Nu_a on the surface of the array enclosure and the higher temperature of the fluid flow within the cluster. Then, for the VSA with $\phi = 0.1162$ ($Da = 2.69 \times 10^{-4}$), the \mathbf{J} fluxes among the gaps between the internal particles are enhanced, exhibiting the similar magnitude of heat transfer in the surrounding fluid flow. This reflects the enhancement of the heat transfer

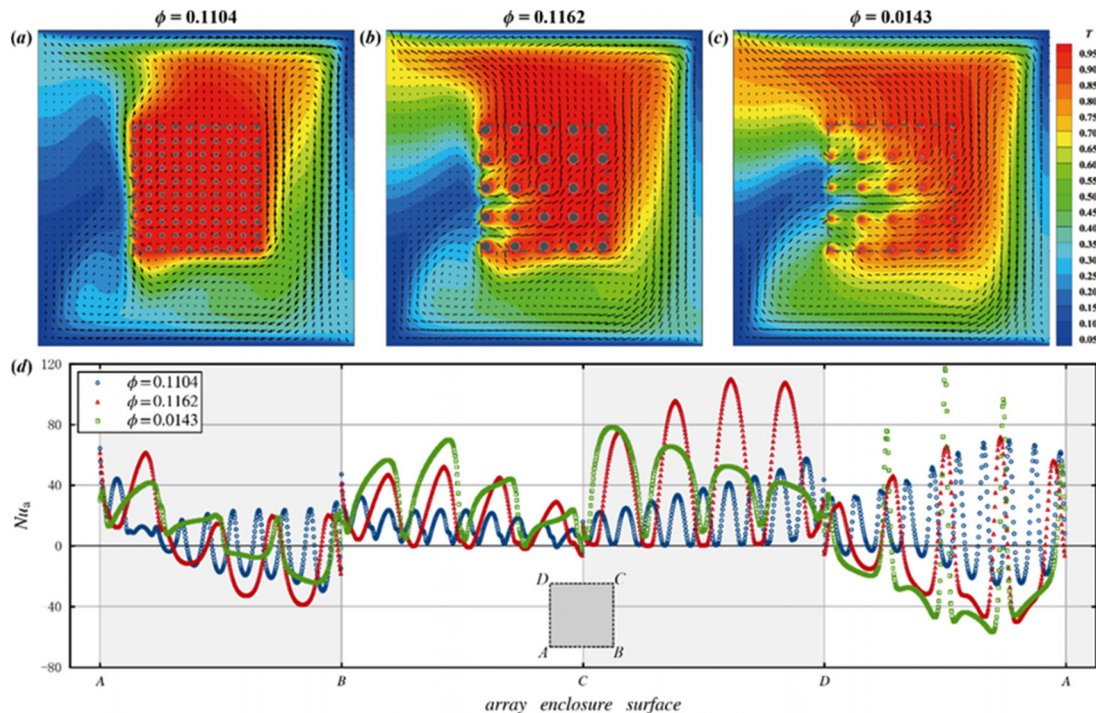


FIG. 14. The heat transfer of the cluster for different arrangements and solid fractions at $Ri = 0.5$: (a)–(c) the isotherms and the total heat flux \mathbf{J} and (d) the local Nusselt number on the surface of array enclosure.

of the cluster. Also, the heat is transferred out of the cluster from edge BC and CD , which increases the temperature of the surrounding fluid flow. Meanwhile, the enhanced convection getting into the array enclosure from the edge DA decreases the temperature of surrounding fluid flow and increases the temperature gradient, thereby enhancing the heat transfer of the interior particles. Despite the solid fraction of cluster being similar to that of the case of VNA with $\phi = 0.1104$, the presence of coarse particle of the VSA with $\phi = 0.1162$ results in the larger inter-particle gaps. Hence, the heat convection in the cluster is promoted, and thus, the Nu_a and \overline{Nu}_a of the cluster are increased. This also demonstrates the limitation of the solid fraction or the porosity to characterize the permeable media, instead, the permeability emerges as a crucial factor that warrants further consideration. Finally, for the VSA with $\phi = 0.0143$ ($Da = 3.02 \times 10^{-3}$), the similar temperature field and J flux distribution can be observed compared to the case of $\phi = 0.1162$, the finer particles lead to the high porosity and permeability of the cluster, enhancing the convection entering the array enclosure from edge DA . The small surface area of the particles results in the inadequate heat generation, causing the reduction in Nu_a along the edge CD . Hence, although the enhanced convection due to the higher permeability promotes the increase in \overline{Nu}_a , the heat transfer performance of the cluster is still limited by the surfaced area of the particles, particularly at the high permeability. The competition of the permeability and surface area induces the optimal condition of permeability for the total averaged Nusselt number \overline{Nu}_a of the cluster. Hence, \overline{Nu}_a first increases but then decreases with Da as shown in Fig. 13. Moreover, it shows that the optimal Da decreases with the increase in Ri according to Fig. 13. This can be explained by the fact that the higher convection within the cluster at larger Ri promotes the transfer of heat out of the cluster, enhancing the demand of heat generated by the particles. Thus, the surface area of the particles could more readily limit the heat transfer performance of the particle cluster.

3. The correlation of Nusselt number

The prediction of the heat transfer performance of the particle cluster is of significant importance in the particle-laden two-phases flow with thermal effects.^{8,57,58} For example, Tang *et al.*¹⁷ developed the linear correlation of the averaged total Nusselt number in relation to the Richardson number and the solid fraction for fluid flow passing through the array of solids. In the present work, the fully-resolved numerical data also raises the well-fitted correlations of \overline{Nu}_a of cluster in the confined flow with respect to Ri and Da . The increase in \overline{Nu}_a with Ri for the lower $Ri \leq 0.4$ in Fig. 8 could be described by a quadratic polynomial as follows:

$$\overline{Nu}_a = a + bRi + cRi^2, \quad (32)$$

where a , b , and c are parameters that correlate with Da . Besides, the tendency of \overline{Nu}_a varying with $\lg(Da)$ in Fig. 13 indicates the cubic polynomial model as follows:

$$\overline{Nu}_a = A + B\lg(Da) + C\lg(Da)^2 + D\lg(Da)^3, \quad (33)$$

where A , B , C , and D are the parameters relating to Ri . Hence, the correlation of \overline{Nu}_a can be modeled using a polynomial correlation involving Ri and $\lg(Da)$. That is to say, the parameters in Eq. (33) could be expanded as the quadratic polynomial formula as shown in Eq. (32), namely,

TABLE III. The fitting results of the correlation of \overline{Nu}_a to Ri and $\lg(Da)$.

ϕ	ϕ_0	ϕ_1	ϕ_2
A	-4.69	-0.149	0.0097
B	-65.80	-0.101	0.0405
C	-278.780	10.495	-0.4413
D	-284.74	23.392	3.2257

$$\psi = \psi_0 + \psi_1 Ri + \psi_2 Ri^2, \quad (34)$$

where ψ indicates the parameters of A , B , C , and D . A curve fitting is implemented and the results of the parameters are listed in Table III. The heat transfer performance of the cluster can thus be predicted using the correlation of \overline{Nu}_a obtained from the fitting, and the results are compared to the fully-resolved simulation as shown in Fig. 15 with an average deviation of 9.2%. The predicted results closely align with the diagonal, demonstrating the reliability of the correlation.

The correlation of \overline{Nu}_a provides a simple way to estimate the heat transfer performance of the particle cluster in a two-sided lid-driven cavity flow. The effect of Ri is first considered, which reflects the competition of forced and natural convections. In addition, the correlation of \overline{Nu}_a is the function of Da , or in other words, is the function of ϕ and d corresponding to the different arrangements of the particle clusters. Note the Darcy number Da is calculated based on the permeability of the cluster estimated by the Carman-Kozeny equation, which could be not very applicable for very dilute clusters of bodies, especially for the flow with nonnegligible inertial force. However, the fluid flow that penetrates the cluster is actually very weak. Inspired by Tang *et al.*,²⁹ the Reynolds number Re_a can be defined as

$$Re_a = \frac{U_a D}{\nu}, \quad (35)$$

where U_a is the Eulerian averaged velocity in the array enclosure, which is calculated by

$$U_a = \frac{1}{V_a(1-\phi)} \int_{V_a-V_b} |\mathbf{u}| dV, \quad (36)$$

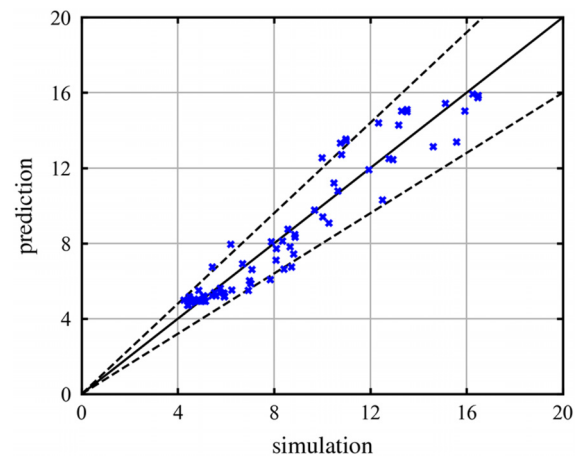


FIG. 15. The prediction values of Eq. (33) combined with Eq. (34) vs the simulation results. The dashed lines correspond to the relative error of $\pm 20\%$.

where V_a and V_b are the volume (cross-sectional area) of the array enclosure and particles. The cases of d/L equaling to 0.0108 and 0.0741, corresponding to the highest and lowest solid fractions studied in the present work, results in $Re_a = 0.7187$ and $Re_a = 1.8617$, respectively, for the Richardson number of 1.0. Hence, the flow inertia within the cluster is quite small, which could improve the applicability of the Carman–Kozeny equation in the present work.

However, it should be pointed out that arrangements of the arrays, such as the distribution modes of the primary particles and the shape of the clusters, could cause the differences in the cluster permeabilities. In such cases, the Carman–Kozeny equation may not accurately predict the permeabilities. To develop more accurate correlations of the heat transfer of the particle clusters, it is essential to accurately determine the permeability of the cluster. Darcy's law provides *a posteriori* way, in which the fluid and temperature fields should be obtained forehand.²⁹ To establish the more accurate and general model of the permeability for the particle clusters with various arrangements, a large amount of the particle-resolved simulation data and theoretical derivations are required. This an important focus in our future endeavors.

The present work has conducted numerical simulations to investigate the heat transfer of single clusters that are formed by the arrays of primary solid particles with various arrangement in the confined fluid flow. The effects of thermal buoyancy (quantified by Ri) and cluster permeability (quantified by ϕ and Da) are discussed. The increase in Ri could enhance the heat transfer performance of the cluster, while the cavity walls limit the increase in the total averaged Nusselt number of the cluster, especially for the high Ri . In addition, it shows that the Darcy number Da correlates well with the variation of \overline{Nu}_a , compared to the solid fraction ϕ (or the porosity) of the cluster. Such aspect is also validated by the corresponding simulations at REV scale. Quite a few previous research only consider the effects porosity on the heat transfer of the cluster¹³ or the fixed bed,^{7,8} which could result in the deviations due to the various arrangements of the particles. Furthermore, the correlation of the \overline{Nu}_a with respect to Ri and Da is developed based on results of the particle-resolved simulations. The effect of permeability of particle cluster on the heat transfer is concluded by the present two-dimensional study, which could still make senses for the three-dimensional configurations. It should be pointed out that the effect of the cavity wall to the heat transfer should be taken into account with the higher Ri . In addition, our current work focused on the stationary clusters. However, the dynamic structure of clusters, which may result in some more complex fluid–particle interactions, thus complicated fluid flow and heat transfer phenomena.^{13,59} Addressing these aspects will be a key focus of our future work.

VI. CONCLUSIONS

In this work, we present a two-dimensional numerical study of the heat transfer and fluid flow in the two-sided lid-driven cavity containing a hot cluster formed by an array of center-placed solids by use of a particle-resolved double distribution function lattice Boltzmann method. The effects of the Richardson number ($Ri = 0.01$ – 1.00) and solid fraction ($\phi = 0.0143$ – 0.6734) were investigated, with the fixed Reynolds number $Re = 1000$ and Prandtl number $Pr = 0.7$. Meanwhile, we focused on the influence of the porous structure of particle cluster by varying the arrangements of solids, and introduced the Darcy number Da to evaluate the permeability of the clusters.

It is found that, with the increase in Ri , the buoyancy induced convection breaks the symmetry of the streamlines and isotherms

around the cluster. The total averaged Nusselt number \overline{Nu}_a is enhanced with the increase in Ri . At high ϕ the particle cluster exhibits similar features, in terms of heat transfer and surrounding fluid flow, to those of single solid rectangle, while at low ϕ it would lead to strong convection in the cluster embodied. In addition, it shows that the Darcy number Da correlates well with the variation of \overline{Nu}_a , in contrast to the solid fraction ϕ (or the porosity) of the cluster. This is also validated by the corresponding simulations at the REV scale. The increase in cluster permeability could significantly alter the heat transfer, resulting in an initial increase followed by a decrease in \overline{Nu}_a as Da increases. This can be explained that the higher permeability could significantly enhance the heat transfer in the cluster, but the insufficient surface area of the particles could limit the heat transfer performance. It is also shown that an empirical correlation of \overline{Nu}_a with regard to Ri and Da could be developed based on the two-dimensional simulation results, allowing the estimation of heat transfer of particle cluster in a confined flow in a simple yet effective way.

ACKNOWLEDGMENTS

The authors would like to thank the National Natural Science Foundation of China (Nos. 22293021, 21991093, and 22288101) for supporting this work.

AUTHOR DECLARATIONS

Conflict of Interest

The authors have no conflicts to disclose.

Author Contributions

Yunxin Zhang: Conceptualization (lead); Data curation (lead); Formal analysis (lead); Investigation (lead); Software (lead); Validation (lead); Writing – original draft (lead). **Chengcong Li:** Investigation (equal); Software (equal); Supervision (equal); Writing – review & editing (equal). **Mao Ye:** Funding acquisition (lead); Project administration (lead); Resources (lead); Supervision (equal); Writing – review & editing (equal).

DATA AVAILABILITY

The data that support the findings of this study are available from the corresponding author upon reasonable request.

APPENDIX: THE LBM FOR VOLUME-AVERAGED EQUATIONS IN REV SCALE

The volume-averaged macroscopic equations, obtained by averaging the microscopic equations over a representative elementary volume (REV), are utilized to describe the heat and fluid flow in the porous media. The equations can be solved using an LBM framework.^{32,33} The corresponding double distribution function lattice Boltzmann equations are written as

$$f_i(\mathbf{r} + \mathbf{e}_i \delta_t, t + \delta_t) - f_i(\mathbf{r}, t) = -\frac{1}{\tau_f} [f_i(\mathbf{r}, t) - f_i^{eq}(\mathbf{r}, t)] + \delta_t F_i(\mathbf{r}, t), \quad (A1)$$

$$g_i(\mathbf{r} + \mathbf{e}_i \delta_t, t + \delta_t) - g_i(\mathbf{r}, t) = -\frac{1}{\tau_g} [g_i(\mathbf{r}, t) - g_i^{eq}(\mathbf{r}, t)] + \delta_t P_i(\mathbf{r}, t), \quad (A2)$$

where the equilibrium distribution function f_i^{eq} and g_i^{eq} are defined as

$$f_i^{eq} = \omega_i \left[\rho + \rho_0 \left(3 \frac{\mathbf{e}_i \cdot \mathbf{u}}{c^2} + 4.5 \frac{(\mathbf{e}_i \cdot \mathbf{u})^2}{c^4} - 1.5 \frac{\mathbf{u}^2}{c^2} \right) \right], \quad (\text{A3})$$

$$g_i^{eq} = \begin{cases} \sigma \rho c_p T - \gamma T + \omega_i \gamma T & i = 0, \\ \omega_i T \left(\gamma + \rho c_p \frac{(\mathbf{e}_i \cdot \mathbf{u})}{c_s^2} \right) & i \neq 0, \end{cases} \quad (\text{A4})$$

where \mathbf{u} and T are volume-averaged velocity and temperature, and γ is a free parameter. $\sigma = [\varepsilon(\rho c_p)_f + (1 - \varepsilon)(\rho c_p)_s] / (\rho c_p)_f$ is the heat capacity ratio, which indicates the relative thermal capacities of the fluid and porous media. The discrete forcing term F_i and P_i are calculated by

$$F_i(\mathbf{r}, t) = \left(1 - \frac{1}{2\tau_f} \right) \omega_i \left[\frac{\mathbf{e}_i - \mathbf{u}}{c_s^2} + \frac{\mathbf{e}_i \cdot \mathbf{u}}{c_s^4} \mathbf{e}_i \right] \cdot \mathbf{F}, \quad (\text{A5})$$

$$P_i(\mathbf{r}, t) = S u_i(\mathbf{r}, t) + Q_i(\mathbf{r}, t), \quad (\text{A6})$$

$$S u_i(\mathbf{r}, t) = \left(1 - \frac{1}{2\tau_g} \right) \omega_i \frac{\mathbf{e}_i}{c_s^2} \cdot \frac{\partial(\rho c_p T \mathbf{u})}{\partial t}, \quad (\text{A7})$$

$$Q_i(\mathbf{r}, t) = \left(1 - \frac{1}{2\tau_g} \right) \omega_i \left(1 + \frac{\mathbf{e}_i \cdot \mathbf{u}}{\sigma \rho c_p c_s^2} \right) Q, \quad (\text{A8})$$

where \mathbf{F} and Q are the body force and heat source. The macroscopic variables can be calculated as

$$\rho = \sum_{i=0}^8 f_i, \quad (\text{A9})$$

$$\rho \mathbf{u} = \sum_{i=0}^8 \mathbf{e}_i f_i + \frac{\delta t}{2} \mathbf{F}, \quad (\text{A10})$$

$$\sigma \rho c_p T = \sum_{i=0}^8 g_i + \frac{\delta t}{2} Q. \quad (\text{A11})$$

A heat source term is implemented to fulfill the fixed temperature of the porous block within the region occupied by the porous block, which is written as $Q = 2\sigma \rho c_p (T_h - T) / \delta t$. The body force due to the presence of porous media is defined as

$$\mathbf{F} = -\frac{\varepsilon \nu_f}{K} \mathbf{u} - \frac{\varepsilon F_e}{\sqrt{K}} |\mathbf{u}| \mathbf{u} + \varepsilon \mathbf{G}, \quad (\text{A12})$$

where $K = \varepsilon^3 d_e^2 / [150(1 - \varepsilon^2)]$ and $F_e = 1.75 / \sqrt{150\varepsilon^3}$ are the permeability and the Forchheimer form coefficient, respectively. \mathbf{G} is the external body force such as the buoyant force based on Boussinesq approximation. The fluid velocity \mathbf{u} can thus be calculated through

$$\mathbf{u} = \frac{\mathbf{V}}{d_0 + \sqrt{d_0^2 + d_1 |\mathbf{V}|}}, \quad \mathbf{V} = \frac{1}{\rho} \sum_{i=0}^8 \mathbf{e}_i f_i + \frac{\delta t}{2} \mathbf{G}, \quad (\text{A13})$$

the parameters d_0 and d_1 are

$$d_0 = \frac{1}{2} \left(1 + \varepsilon \frac{\delta \nu_f}{2K} \right), \quad d_1 = \varepsilon \frac{\delta F_e}{2K}. \quad (\text{A14})$$

The lattice Boltzmann equations can be related to the volume-averaged macroscopic equations,^{32,33} and the relaxation times can thus be given as

$$\nu_e = c_s^2 \left(\tau_f - \frac{1}{2} \right) \delta t, \quad \chi_e = \gamma c_s^2 \left(\tau_g - \frac{1}{2} \right) \delta t, \quad (\text{A15})$$

where $\nu_e = J_e \nu_f$ is the effective kinematic viscosity, J_e is the viscosity ratio. $\chi_e = \alpha_e (\rho c_p)_f = \varepsilon \chi_f + (1 - \varepsilon) \chi_s$ is the effective thermal conductivity, relating to the thermal conductivities χ_f and χ_s of the fluid flow and porous media.

REFERENCES

- G. Yue, R. Cai, J. Lu, and H. Zhang, "From a CFB reactor to a CFB boiler—The review of R&D progress of CFB coal combustion technology in China," *Powder Technol.* **316**, 18 (2017).
- J. Mellmann, "The transverse motion of solids in rotating cylinders—forms of motion and transition behavior," *Powder Technol.* **118**, 251 (2001).
- J. J. Derksen, "Solid particle mobility in agitated Bingham liquids," *Ind. Eng. Chem. Res.* **48**, 2266 (2009).
- W. Ge, Q. Chang, C. Li, and J. Wang, "Multiscale structures in particle–fluid systems: Characterization, modeling, and simulation," *Chem. Eng. Sci.* **198**, 198 (2019).
- M. Saruwatari and H. Nakamura, "Coarse-grained discrete element method of particle behavior and heat transfer in a rotary kiln," *Chem. Eng. J.* **428**, 130969 (2022).
- L. Kong, J. Xu, J. Wang, and W. Ge, "Characterizing particle clustering behavior in dense gas–solid suspensions," *Ind. Eng. Chem. Res.* **62**, 19145 (2023).
- Y. Chen and C. R. Müller, "Lattice Boltzmann simulation of gas–solid heat transfer in random assemblies of spheres: The effect of solids volume fraction on the average Nusselt number for $Re \leq 100$," *Chem. Eng. J.* **361**, 1392 (2019).
- Z. Qi and A. B. Yu, "A new correlation for heat transfer in particle–fluid beds," *Int. J. Heat Mass Transfer* **181**, 121844 (2021).
- L. Wang, C. Wu, and W. Ge, "Effect of particle clusters on mass transfer between gas and particles in gas–solid flows," *Powder Technol.* **319**, 221 (2017).
- Z. Cao and D. K. Tafti, "Convective heat transfer in suspensions of prolate ellipsoids," *Int. J. Heat Mass Transfer* **177**, 121575 (2021).
- J. Fu, S. Chen, P. Chen, and C. Wen, "Particle-resolved simulation on viscous flow past random and ordered arrays of hot ellipsoidal particles," *Int. J. Multiphase Flow* **142**, 103736 (2021).
- A. Nicolle and I. Eames, "Numerical study of flow through and around a circular array of cylinders," *J. Fluid Mech.* **679**, 1–31 (2011).
- S. Wang, G. Liu, Y. Wu, J. Chen, Y. Liu, and L. Wei, "Numerical investigation of gas-to-particle cluster convective heat transfer in circulating fluidized beds," *Int. J. Heat Mass Transfer* **53**, 3102 (2010).
- K. Wittig, A. Golia, and P. A. Nikrityuk, "3D numerical study on the influence of particle porosity on heat and fluid flow," *Prog. Comput. Fluid Dyn.* **12**, 207 (2012).
- S. Ganguli and S. K. Lele, "Drag of a heated sphere at low Reynolds numbers in the absence of buoyancy," *J. Fluid Mech.* **869**, 264 (2019).
- H. Gan, J. Chang, J. J. Feng, and H. H. Hu, "Direct numerical simulation of the sedimentation of solid particles with thermal convection," *J. Fluid Mech.* **481**, 385 (2003).
- T. Tang, Z. Li, S. Yu, J. Li, and P. Yu, "Opposing-buoyancy mixed convection through and around arrays of heated cylinders," *J. Fluid Mech.* **949**, A8 (2022).
- J. Fu, S. Chen, and X. Zhou, "Effect of heterogeneity on interphase heat transfer for gas–solid flow: A particle-resolved direct numerical simulation," *Phys. Fluids* **34**, 123317 (2022).
- P. N. Shankar and M. D. Deshpande, "Fluid mechanics in the driven cavity," *Annu. Rev. Fluid Mech.* **32**, 93 (2000).
- K. Khanafer, S. M. Aithal, M. E. Assad, and I. Pop, "Flow and heat transfer in a driven cavity with two cylinders," *J. Thermophys. Heat Transfer* **31**, 99 (2017).
- K. M. Gangawane, "Computational analysis of mixed convection heat transfer characteristics in lid-driven cavity containing triangular block with constant heat flux: Effect of Prandtl and Grashof numbers," *Int. J. Heat Mass Transfer* **105**, 34 (2017).
- K. M. Gangawane, H. F. Oztop, and N. Abu-Hamdeh, "Mixed convection characteristic in a lid-driven cavity containing heated triangular block: Effect of location and size of block," *Int. J. Heat Mass Transfer* **124**, 860 (2018).

- ²³S. Taghizadeh and A. Asaditaheri, "Heat transfer and entropy generation of laminar mixed convection in an inclined lid driven enclosure with a circular porous cylinder," *Int. J. Therm. Sci.* **134**, 242 (2018).
- ²⁴D. Kashyap and A. K. Dass, "Influence of cavity inclination on mixed convection in a double-sided lid-driven cavity with a centrally inserted hot porous block," *Int. J. Therm. Sci.* **181**, 107732 (2022).
- ²⁵A. A. Merrikh and J. L. Lage, "Natural convection in an enclosure with disconnected and conducting solid blocks," *Int. J. Heat Mass Transfer* **48**, 1361 (2005).
- ²⁶S. Liu, L. Jiang, K. L. Chong, X. Zhu, Z.-H. Wan, R. Verzicco, R. J. A. M. Stevens, D. Lohse, and C. Sun, "From Rayleigh-Bénard convection to porous-media convection: How porosity affects heat transfer and flow structure," *J. Fluid Mech.* **895**, A18 (2020).
- ²⁷Y. Zhang, C. Li, and M. Ye, "Motion of a two-dimensional neutrally buoyant circular particle in two-sided lid-driven cavity flow with thermal convection," *Phys. Fluids* **35**, 123305 (2023).
- ²⁸T. Tang, P. Yu, X. Shan, and H. Chen, "The formation mechanism of recirculating wake for steady flow through and around arrays of cylinders," *Phys. Fluids* **31**, 043607 (2019).
- ²⁹T. Tang, P. Yu, X. Shan, H. Chen, and J. Su, "Investigation of drag properties for flow through and around square arrays of cylinders at low Reynolds numbers," *Chem. Eng. Sci.* **199**, 285 (2019).
- ³⁰J. Bear, *Dynamics of Fluids in Porous Media* (Dover, New York, NY, 1988).
- ³¹L. Ma, S. Xu, X. Li, Q. Guo, D. Gao, Y. Ding, M. Ye, and Z. Liu, "Particle tracking velocimetry of porous sphere settling under gravity: Preparation of the model porous particle and measurement of drag coefficients," *Powder Technol.* **360**, 241 (2020).
- ³²D. Gao, Z. Chen, L. Chen, and D. Zhang, "A modified lattice Boltzmann model for conjugate heat transfer in porous media," *Int. J. Heat Mass Transfer* **105**, 673 (2017).
- ³³L. Wang, L.-P. Wang, Z. Guo, and J. Mi, "Volume-averaged macroscopic equation for fluid flow in moving porous media," *Int. J. Heat Mass Transfer* **82**, 357 (2015).
- ³⁴W. Tao, Y. He, and L. Chen, "A comprehensive review and comparison on heatline concept and field synergy principle," *Int. J. Heat Mass Transfer* **135**, 436 (2019).
- ³⁵S. Kimura and A. Bejan, "The 'heatline' visualization of convective heat transfer," *J. Heat Transfer* **105**, 916 (1983).
- ³⁶V. A. F. Costa, "Unification of the streamline, heatline and massline methods for the visualization of two-dimensional transport phenomena," *Int. J. Heat Mass Transfer* **42**, 27 (1999).
- ³⁷S. Chen and G. D. Doolen, "Lattice Boltzmann method for fluid flows," *Annu. Rev. Fluid Mech.* **30**, 329 (1998).
- ³⁸Y. Peng, C. Shu, and Y. T. Chew, "Simplified thermal lattice Boltzmann model for incompressible thermal flows," *Phys. Rev. E* **68**, 026701 (2003).
- ³⁹X. He and L. Luo, "Lattice Boltzmann model for the incompressible Navier-Stokes equation," *J. Stat. Phys.* **88**, 927 (1997).
- ⁴⁰Z. Guo, C. Zheng, and B. Shi, "Discrete lattice effects on the forcing term in the lattice Boltzmann method," *Phys. Rev. E* **65**, 046308 (2002).
- ⁴¹Z. Guo, C. Zheng, and B. Shi, "An extrapolation method for boundary conditions in lattice Boltzmann method," *Phys. Fluids* **14**, 2007 (2002).
- ⁴²H. Huang, T. S. Lee, and C. Shu, "Thermal curved boundary treatment for the thermal lattice Boltzmann equation," *Int. J. Mod. Phys. C* **17**, 631 (2006).
- ⁴³Z. Guo, C. Zheng, and B. Shi, "Non-equilibrium extrapolation method for velocity and pressure boundary conditions in the lattice Boltzmann method," *Chin. Phys.* **11**, 366 (2002).
- ⁴⁴Z. Guo, C. Zheng, B. Shi, and T. S. Zhao, "Thermal lattice Boltzmann equation for low Mach number flows: Decoupling model," *Phys. Rev. E* **75**, 036704 (2007).
- ⁴⁵I. Demirdžić, Ž. Lilek, and M. Perić, "Fluid flow and heat transfer test problems for non-orthogonal grids: Bench-mark solutions," *Int. J. Numer. Methods Fluids* **15**, 329 (1992).
- ⁴⁶Z. Yu, X. Shao, and A. Wachs, "A fictitious domain method for particulate flows with heat transfer," *J. Comput. Phys.* **217**, 424 (2006).
- ⁴⁷Y. Wang, C. Shu, and C. J. Teo, "Thermal lattice Boltzmann flux solver and its application for simulation of incompressible thermal flows," *Comput. Fluids* **94**, 98 (2014).
- ⁴⁸R. Franke *et al.*, "Numerical calculation of laminar vortex-shedding flow past cylinders," *J. Wind. Eng. Ind. Aerodyn.* **35**, 237 (1990).
- ⁴⁹M. Breuer, J. Bernsdorf, T. Zeiser, and F. Durst, "Accurate computations of the laminar flow past a square cylinder based on two different methods: Lattice-Boltzmann and finite-volume," *Int. J. Heat Fluid Flow* **21**, 186 (2000).
- ⁵⁰B. S. Varaprasad Patnaik, P. A. Aswatha Narayana, and K. N. Seetharamu, "Numerical simulation of vortex shedding past a circular cylinder under the influence of buoyancy," *Int. J. Heat Mass Transfer* **42**, 3495 (1999).
- ⁵¹N. Sharma, A. K. Dhiman, and S. Kumar, "Mixed convection flow and heat transfer across a square cylinder under the influence of aiding buoyancy at low Reynolds numbers," *Int. J. Heat Mass Transfer* **55**, 2601 (2012).
- ⁵²H. M. Badr, "A theoretical study of laminar mixed convection from a horizontal cylinder in a cross stream," *Int. J. Heat Mass Transfer* **26**, 639 (1983).
- ⁵³K. Chang and J. Y. Sa, "The effect of buoyancy on vortex shedding in the near wake of a circular cylinder," *J. Fluid Mech.* **220**, 253 (1990).
- ⁵⁴A. W. Islam, M. A. R. Sharif, and E. S. Carlson, "Mixed convection in a lid driven square cavity with an isothermally heated square blockage inside," *Int. J. Heat Mass Transfer* **55**, 5244 (2012).
- ⁵⁵J. Liu, C. Li, M. Ye, and Z. Liu, "The rotation of two-dimensional elliptical porous particles in a simple shear flow with fluid inertia," *Phys. Fluids* **32**, 043305 (2020).
- ⁵⁶C. Li, M. Ye, and Z. Liu, "On the rotation of a circular porous particle in 2D simple shear flow with fluid inertia," *J. Fluid Mech.* **808**, R3 (2016).
- ⁵⁷N. G. Deen, E. A. J. F. Peters, J. T. Padding, and J. A. M. Kuipers, "Review of direct numerical simulation of fluid-particle mass, momentum and heat transfer in dense gas-solid flows," *Chem. Eng. Sci.* **116**, 710 (2014).
- ⁵⁸L. Zhu, Y. Liu, and Z. Luo, "An enhanced correlation for gas-particle heat and mass transfer in packed and fluidized bed reactors," *Chem. Eng. J.* **374**, 531 (2019).
- ⁵⁹J. Hu and Z. Guo, "Effect of interaction between a particle cluster and a single particle on particle motion and distribution during sedimentation: A numerical study," *Phys. Fluids* **31**, 033301 (2019).